Eur. Phys. J. B **31**, 495–507 (2003)
DOI: 10.1140/epjb/e2003-00059-9

THE EUROPEAN PHYSICAL JOURNAL B

# The normal state scattering rate in high-$T_c$ cuprates

N.E. Hussey[a]

H.H. Wills Physics Laboratory, University of Bristol, Bristol, BS8 1TL, UK

Received 5 June 2002 / Received in final form 17 December 2002
Published online 6 March 2003 – 

**Abstract.** A detailed phenomenological model is developed for the normal state transport properties of optimal and overdoped high-$T_c$ cuprates. In particular, an explicit form of scattering rate is identified that may account, qualitatively and quantitatively, for the normal state (magneto)-transport properties of $Tl_2Ba_2CuO_{6+\delta}$ and $Bi_2Sr_2CaCu_2O_{8+\delta}$ across the overdoped side of the phase diagram. The proscribed form of the scattering rate is consistent also with features seen in the photoemission spectroscopy of $Bi_2Sr_2CaCu_2O_{8+\delta}$ and offers a new and intuitive way to understand the evolution of the temperature dependence of the inverse Hall angle in Bi-based cuprates with carrier concentration.

**PACS.** 72.10.-d Theory of electronic transport; scattering mechanisms – 74.25.Fy Transport properties (electric and thermal conductivity, thermoelectric effects, etc.) – 74.72.Fq Tl-based cuprates

## 1 Introduction

The search for a consistent description for the anomalous normal state transport properties of high-$T_c$ cuprates (HTSC) has been a long and challenging journey. Many phenomenological models seeking to identify the appropriate form for the normal state scattering rate have been offered but none seem to have captured the entire picture. From the beginning, it was clear that the $T$-linear behaviour of the in-plane resistivity $\rho_{ab}$, extending over an anomalously broad range of temperature for optimally doped (OP) cuprates, would be difficult to reconcile within a conventional Fermi-liquid (FL) framework [1]. Later observations of the $T^2$ dependence and impurity dependence of the inverse Hall angle $\cot\Theta_H$ [2], together with a modified Kohler's rule (in-plane orbital magnetoresistance (MR) $\Delta\rho_{ab}/\rho_{ab} \sim \tan^2\Theta_H$) [3], seemed to present an insurmountable challenge to FL theory.

Several notable attempts to explain the anomalous transport behaviour of HTSC within a modified FL scenario followed, each incorporating some particular form for the (strong) anisotropy of the transport scattering rate within the $CuO_2$ plane arising out of some form of coupling to a singular bosonic mode, be it that of spin fluctuations [4,5], charge fluctuations [6] or $d$-wave superconducting fluctuations [7]. In each case, however, inconsistencies towards certain aspects of the experimental data were exposed.

Given these failings, other more exotic models, based on a non-FL ground state, gained prominence within the community; most notably the two-lifetime picture of Anderson [8] and the Marginal-Fermi-liquid (MFL) model of Varma and co-workers [9,10]. Two-lifetime modelling has been extremely insightful for understanding the experimental situation in OP cuprates, but has yet failed to provide an explanation for the results of Angle-Resolved Photoemission Spectroscopy (ARPES) or indeed the evolution of the transport phenomena with doping. The MFL hypothesis assumes optimum $T_c$ to lie in proximity to a quantum critical point and consequently, quasi-particles are ill-defined everywhere on the Fermi surface, with a self-energy that is governed simply by the temperature (or frequency) scale. In contrast to the two-lifetime picture, the MFL model is consistent with certain aspects of ARPES measurements [11], though not all. Most notably, the recently reported evidence of a kink in the energy dispersion [12] seems at odds with a scenario based on quantum criticality. Yet again, predictions of the MFL theory have been largely confined to optimal doping.

In this paper, I set out a new phenomenology for the normal state scattering rate in HTSC that offers an alternative approach to understanding these various anomalies. In Section 2, the salient features of the model are presented. The modelling has as its basis, two novel assumptions. Firstly, the dominant scattering rate is taken to vary as $T^2$ everywhere on the Fermi surface, but in contrast to previous approaches, both the impurity *and* the electronic scattering terms contain strong (doping dependent) basal plane anisotropy. The second key assumption is that this anisotropic scattering rate saturates eventually (on different parts of the Fermi surface at different temperatures) at a value equivalent to the Mott-Ioffe-Regel criterion for coherent band transport. In

[a] e-mail: n.e.hussey@bristol.ac.uk

Section 3.1, the model is compared with extensive experimental data on $Tl_2Ba_2CuO_{6+\delta}$ (Tl2201) at different doping concentrations. Excellent qualitative and quantitative agreement is found between the model and experimental data for $\rho_{ab}(T)$, $\cot\Theta_H(T)$ and most significantly, for the magnitude and $T$-dependence of $\Delta\rho_{ab}/\rho_{ab}(T)$, with relatively few fitting parameters. The model goes beyond previous proposals in that it can account also for the evolution of the observed normal state behaviour from optimum doping through to the heavily overdoped (OD) region of the phase diagram. To conclude this section, the effects of disorder on $\rho_{ab}(T)$ and $\cot\Theta_H(T)$ in OP Tl2201 are also considered. In Section 3.2, the model is applied to quasi-particle scattering rate data (derived from recent ARPES measurements) and to normal state transport data for $Bi_2Sr_2CaCu_2O_{8+\delta}$ (Bi2212), with reference being made to single-layered $Bi_2Sr_{2-x}La_xCuO_{6+\delta}$ (Bi2201). In particular, the model is shown to provide a natural explanation for the *non*-universal power law behaviour of $\cot\Theta_H(T)$ observed in these Bi-based cuprates [13,14]. Finally, in Section 4, some physical justification for the particular form of scattering is presented and the implications of our phenomenological model for the physics of HTSC across the phase diagram are highlighted. In the process, two of the previously established paradigms of the normal state in HTSC are challenged; namely the linear low-$T$ behaviour of $\rho_{ab}(T)$ and the relevance of the non-saturating $\rho_{ab}(T)$ observed in certain circumstances at higher temperatures.

## 2 The model

There is strong experimental evidence from both ARPES [15] and $c$-axis MR [16] that the dominant scattering in HTSC is highly anisotropic within the basal plane, being most intense at the so-called 'anti-nodal' points at ($\pi$, 0) and weakest at the nodal points ($\pi$, $\pi$). Moreover, this basal plane anisotropy is found to grow weaker with overdoping [15]. The $c$-axis MR measurements, carried out on OD Tl2201 ($T_c$ = 30 K) [16], revealed that this basal plane anisotropy is also $T$-dependent and can account, qualitatively at least, for the slight but still significant 'separation of lifetimes' observed in $\rho_{ab}(T)$ and $\cot\Theta_H(T)$ at this particular hole concentration.

In a 2D metal with an anisotropic in-plane mean-free-path, Ong has shown how the Hall angle $\tan\Theta_H(T)$ will be dominated by those regions of the Fermi surface where the scattering is weakest [17]. If the anisotropy is sufficiently high, $\cot\Theta_H(T)$ will simply reflect the $T$-dependence of the scattering rate of the most mobile carriers. Given that in the majority of cuprates, $\cot\Theta_H(T) \sim A + BT^2$, I infer this to represent the *intrinsic* $T$-dependence of the (dominant) scattering process at the nodal points. A key stipulation of the present model is that this $T^2$ scattering rate is manifest *everywhere* on the Fermi surface, but has four-fold basal plane symmetry and is maximal along ($\pi$, 0). Combined with an elastic scattering rate $\Gamma_0(\phi)$, that may also contain 4-fold anisotropy [10], an 'ideal' scattering rate $\Gamma_{\rm ideal}(\phi)$ is then proposed,

$$\Gamma_{\rm ideal}(\phi) = \Gamma_0(\phi) + \Gamma_T(\phi)$$

where

$$\Gamma_0(\phi) = \alpha(1 + c\cos^2 2\phi)$$

and the $T$-dependent scattering rate

$$\Gamma_T(\phi) = \beta(1 + e\cos^4 2\phi)T^2.$$

Here $\phi$ represents the angle between the in-plane Fermi wave vector and ($k_x$, 0) whilst $c$ and $e$ are the doping-dependent anisotropy factors for the impurity and $T$-dependent scattering rates respectively. The coefficients $\alpha$ and $\beta$ should approximate $A$ and $B$ from the $T$-dependence of $\cot\Theta_H(T)$. The particular angular dependencies chosen for $\Gamma_0(\phi)$ and $\Gamma_T(\phi)$ exhibit the appropriate four-fold anisotropy but show different curvature around the Fermi surface, in agreement with subsequent analysis of ARPES data in Bi2212, as highlighted in Section 3.2 and shown explicitly in Figure 7. Note that $\Gamma_{\rm ideal}(\phi)$ is largest ($=\alpha(1 + c) + \beta(1 + e)T^2$) along ($\pi$, 0) and smallest, but still finite ($=\alpha+\beta T^2 \sim A+BT^2$), along ($\pi$, $\pi$).

The second key feature of the model is the application of the Mott-Ioffe-Regel (MIR) limit. In its basic form, the MIR criterion states that the quasi-particle mean free path $\ell$ cannot become smaller than the lattice spacing $a$, since at this point, the quasi-particles lose their coherence and conventional Boltzmann transport analysis breaks down. When $k$-dependence is introduced, different regions of the Fermi surface become incoherent at different temperatures. Likewise, the scattering rate at different points on the Fermi surface will saturate (at the MIR limit) at different temperatures.

Early evidence for resistivity saturation in metals, consistent with the MIR limit, was reported in the A-15 superconductors [18]. The $T$-dependence of the resistivity was found to fit extremely well to a simple 'parallel-resistor' model [19], suggesting that the ideal resistivity (*i.e.* in the absence of saturation) was somehow shunted by a large saturation resistivity $\rho_{\rm max}$ corresponding to $\ell = a$. Using the MIR criterion as his guide, Gurvitch later derived an elegant understanding of the appropriateness of the parallel-resistor model for resistivity saturation [20]. Gurvitch argued that there must be a minimum time $\tau_0$ below which no scattering event can take place, *i.e.* a minimum distance $a$ over which each carrier gains additional drift velocity before being scattered. By including $\tau_0$ in the probability distribution for electron scattering, Gurvitch uncovered an additional term in the expression for drift velocity (and hence the conductivity) containing a minimum lifetime (maximum scattering rate) equivalent to the MIR criterion. Upon inverting this new conductivity expression, one naturally arrives then at the parallel-resistor form for resistivity saturation.

In the spirit of Gurvitch's picture, I introduce for HTSC a maximum scattering rate (minimum lifetime) $\Gamma_{\rm max}(\phi)$, equivalent to $\ell = a$, and define an *effective*

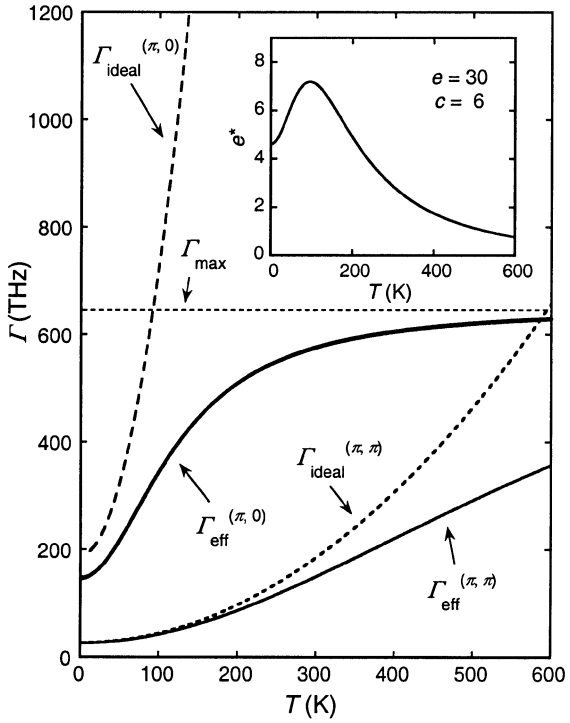


**Fig. 1.** $T$-dependencies of the ideal and effective scattering rates for the $(\pi, 0)$ and $(\pi, \pi)$ quasi-particles in OP Tl2201. The parameters used are given in the text. Inset: $T$-dependence of the effective anisotropy $e^* = {\Gamma_{\rm eff}}^{(\pi,0)}/{\Gamma_{\rm eff}}^{(\pi,\pi)} - 1$ for the same parameters indicated.

scattering rate $\Gamma_{\rm eff}(\phi)$ at each point on the Fermi surface of the parallel-resistor form, *i.e.*

$$\frac{1}{\Gamma_{\rm eff}(\phi)} = \frac{1}{\Gamma_{\rm ideal}(\phi)} + \frac{1}{\Gamma_{\rm max}(\phi)}.$$

$\Gamma_{\rm eff}(\phi)$ is now inserted into the Jones-Zener expansion of the linearised Boltzmann transport equation (BTE) for a quasi-2D Fermi surface to extract all measurable transport coefficients. A derivation of the appropriate expressions is included as an Appendix. Since the Fermi velocity $v_F$ ($= 1$–$3 \times 10^5$ ms$^{-1}$) is already well established through ARPES measurements, the value $\Gamma_{\rm max}$ can be fixed directly from the MIR criterion ($\ell = a$) giving $\Gamma_{\rm max}$ in the range 250–750 THz (0.16–0.5 eV). As will be shown, this simple phenomenology is sufficient to explain the differing $T$-dependencies that appear in the normal state transport properties of HTSC.

The appropriate $T$-dependencies of $\Gamma_{\rm eff}(\phi, T)$ for the two most relevant momentum directions, $(\pi, 0)$ and $(\pi, \pi)$, are illustrated schematically in Figure 1. For concreteness, the parameters employed in this simulation are those appropriate for OP Tl2201 ($T_c \sim 90$ K), namely $\alpha = 27$ THz, $\beta = 1.75 \times 10^{-3}$ THz/K$^2$, $c = 6$, $e = 30$ and $\Gamma_{\rm max} = 650$ THz. Along $(\pi, 0)$, $\Gamma_{\rm ideal}(T)$ reaches $\Gamma_{\rm max}$ at $T_c \sim 90$ K, at which point the anti-nodal quasi-particles become incoherent. Due to the presence of the 'shunt' $\Gamma_{\rm max}$, however, ${\Gamma_{\rm eff}}^{(\pi,0)}(T)$ is always smaller than ${\Gamma_{\rm ideal}}^{(\pi,0)}(T)$ and approaches saturation much more gradually. For the quasi-particles at $(\pi, \pi)$ on the other hand, $\Gamma_{\rm ideal}(T)$ only reaches $\Gamma_{\rm max}$ at a much higher temperature ($T \sim 600$ K). Hence, at the nodal points, well-defined coherent quasi-particles exist at all relevant temperatures. Note that $\Gamma_{\rm eff}(T)$ at $(\pi, \pi)$ is quasi-linear over a wide temperature range. The 'effective' anisotropy factor $e^*$ ($={\Gamma_{\rm eff}}^{(\pi,0)}/{\Gamma_{\rm eff}}^{(\pi,\pi)} - 1$) is significantly lower than $e$ itself for all finite $T$, reaching a maximum value $\sim$7 at the temperature where ${\Gamma_{\rm ideal}}^{(\pi,0)}$ first crosses $\Gamma_{\rm max}$ (see inset to Fig. 1). The overall effect is a transport scattering rate $\Gamma_{\rm eff}(\phi, T)$ whose anisotropy initially grows with increasing $T$ but then gradually becomes more isotropic at higher temperatures as the scattering rate at broader regions of the Fermi surface tends towards saturation. In this way, the $T$-dependence of $e^*(T)$ reflects that of the Hall coefficient $R_H(T)$ in HTSC.

## 3 Fitting

### 3.1 Application to Tl2201

Tl2201 is an ideal system for modelling the normal state transport properties in HTSC for several important reasons; (i) Tl2201 is a single band cuprate, and moreover does not contain any secondary conducting subsystem, such as the CuO chains that complicate Hall and/or MR data in $YBa_2Cu_3O_{7-\delta}$ (YBCO) for example; (ii) having a single $CuO_2$ plane, bilayer coupling is not an issue; (iii) the doping range of Tl2201 covers only the OP and OD regions of the phase diagram thereby avoiding any additional complications due to the normal state pseudogap; (iv) a $T$-dependent anisotropy in the in-plane scattering rate has already been detected in OD Tl2201 ($T_c = 30$ K) from $c$-axis MR measurements [16]; finally (v) OP Tl2201 exhibits the very clean separation of the ($T$-linear) transport and ($T^2$) Hall lifetimes characteristic of OP cuprates. Experimental $\rho_{ab}(T)$ and $\cot\Theta_H(T)$ data for OP Tl2201 [21,22] are reproduced in Figure 2 as closed circles. One surprising feature of the data is the small *negative* zero-temperature intercept in $\rho_{ab}(T)$ (extrapolation indicated by a dotted line) which coexists with a large *positive* intercept in $\cot\Theta_H(T)$. Line fits to the experimental data between 130 K and 300 K give $\rho_{ab}(T) = -10 + 1.56T$ ($\mu\Omega$cm) and $\cot\Theta_H(T) = 27 + 0.0014T^2$ (in 10 tesla) [22]. This subtle but crucial feature of the data has often been overlooked but is, as will be shown, a natural consequence of the scattering rate formalism presented here.

To complete the Boltzmann transport analysis, I introduce a Fermi wave vector $k_F(\phi)$ and Fermi velocity $v_F(\phi)$ consistent with band structure calculations [23], *viz.* $k_F(\phi) = 0.65(1 + 0.15\sin^2 2\phi)$ Å$^{-1}$ and $v_F(\phi) = 2.5(1 + 0.2\sin^2 2\phi) \times 10^5$ ms$^{-1}$. This expression for $k_F(\phi)$ corresponds to a hole doping concentration $p = 0.16$. These relatively small anisotropy factors do not play a significant role in the following analysis; moreover for simplicity, both $k_F(\phi)$ and $v_F(\phi)$ will be assumed to be independent of doping concentration. The corresponding saturation scattering rate $\Gamma_{\rm max}(\phi) = 650(1 + 0.2\sin^2 2\phi)$ THz

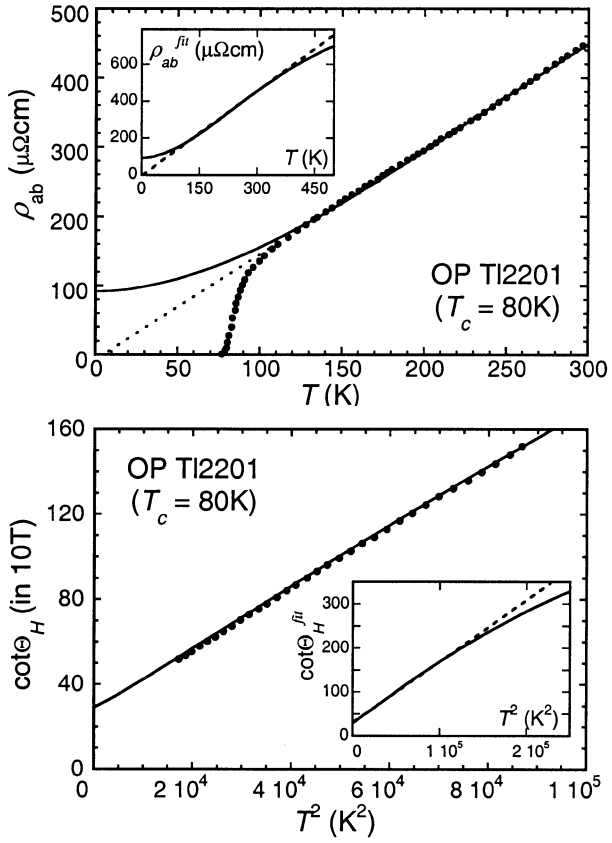


**Fig. 2.** Top: $\rho_{ab}(T)$ (closed circles) and $\rho_{ab}^{fit}(T)$ (solid line) for OP Tl2201 [21]. The dotted line is an extrapolation of $\rho_{ab}(T)$ to $T = 0$ K. Bottom: cot$\Theta_H(T)$ (closed circles) and cot$\Theta_H^{fit}(T)$ for the same crystal [21]. Insets: The same fits taken up to 500 K, showing the onset of saturation at higher $T$.

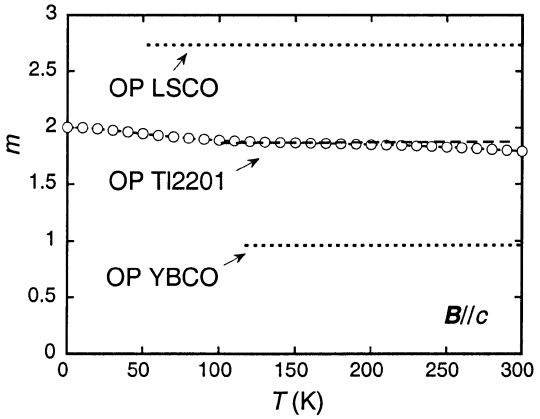


**Fig. 3.** *Dashed line*: Modified Kohler's plot $m(T)$ for OP Tl2201 [22] (where $m^2 = (\Delta\rho_{ab}/\rho_{ab})/tan^2\Theta_H$). The open circles represent $m^{fit}(T)$ obtained with the same fitting parameters as used in Figure 2. *Dotted lines*: $m(T)$ for OP LSCO and YBCO [3].

or $0.45(1 + 0.2\sin^2 2\phi)$ eV (since $a = 3.86$ Å). Note that the value of $\Gamma_{\max}$ is entirely determined by our choice of $v_F$ and contains the same anisotropy factor as $v_F$ to ensure the condition $\ell = a$ is ultimately satisfied everywhere on the Fermi surface. Again, these values are kept constant for all doping concentrations studied here. Thus in the ensuing analysis, there become only four adjustable parameters, namely the two scattering anisotropy parameters $c$ and $e$ and the magnitude coefficients of $\Gamma_{\rm ideal}(T)$, $\alpha$ and $\beta$. The choice of $\alpha$ and $\beta$ is limited however since according to the Ong representation, $\alpha$ and $\beta$ should be comparable with the coefficients $A$ and $B$ determined from cot$\Theta_H(T)$. These four parameters are now adjusted to obtain the best global fits, labelled hereafter $\rho_{ab}^{fit}(T)$, cot$\Theta_H^{fit}(T)$ and $\Delta\rho_{ab}^{fit}/\rho_{ab}^{fit}(T)$, to the three independent transport properties $\rho_{ab}(T)$, cot$\Theta_H(T)$ and $\Delta\rho_{ab}/\rho_{ab}(T)$. Finally, scaling corrections of the order 30% were permitted in the fits to allow for any systematic errors in the absolute magnitudes of the experimentally determined quantities.

The solid lines in Figure 2 are $\rho_{ab}^{fit}(T)$ and cot$\Theta_H^{fit}(T)$ for OP Tl2201. The fitting parameters used here are $\alpha = 27$ THz, $\beta = 0.00175$ THz/K$^2$, $c = 6$ and $e = 30$. Above 130 K, both the linear resistivity and the quadratic Hall angle are reproduced with slopes and (extrapolated) $T = 0$ intercepts in excellent agreement with the experimental data. Below 130 K, $\rho_{ab}^{fit}(T)$ departs from linearity, approaching $T^2$ as $T \to 0$, whilst $\rho_{ab}(T)$ in fact shows a downward deviation from linearity below 130 K, due presumably to the onset of superconducting fluctuations which always dominate the intrinsic behaviour of the normal state $\rho_{ab}(T)$ near $T_c$. Note that the $T$-dependence of cot$\Theta_H(T)$ $(=27 + 0.0014T^2)$ is very similar to that of $\Gamma_{\rm ideal}(T)$ $(=27 + 0.00175T^2)$, in good agreement with Ong's picture [17]. It is interesting to note that the extrapolated value of the residual resistivity ($\rho_0 \approx 90\ \mu\Omega$cm) in OP Tl2201 is comparable with those obtained experimentally for other single-layered OP cuprates, namely $La_{1.83}Sr_{0.17}CuO_4$ ($\rho_0 \approx 110\ \mu\Omega$cm [24]) and OP Bi2201 ($\rho_0 \approx 120\ \mu\Omega$cm [25]), where $T_c$ has been suppressed to very low temperatures by the application of a large pulsed magnetic field.

The insets in Figure 2 show $\rho_{ab}^{fit}(T)$ and cot$\Theta_H^{fit}(T)$ over an extended temperature range up to 500 K. The influence of $\Gamma_{\max}$ on the high-$T$ behaviour is manifest as a deviation from linearity above 360 K, indicating the onset of saturation in $\Gamma_{\rm eff}(T)$. The fact that this tendency towards saturation is not actually observed in $\rho_{ab}(T)$ indicates that the model does not capture all the essential physics. However, as I argue in Section 4, there are several possible factors that might lead to a non-saturating resistivity in HTSC which go beyond conventional Boltzmann transport analysis and which may mask the intrinsic behaviour of the scattering rate at higher temperatures.

The modified Kohler's rule $\Delta\rho_{ab}/\rho_{ab} = m^2\ \tan^2\Theta_H$ is also seen in OP Tl2201, with $m \sim 1.9$ down to 130 K [22], as indicated by the dashed line in Figure 3. (Below this temperature, superconducting fluctuations again begin to dominate.) This value lies in between the experimentally determined values for OP $La_{2-x}Sr_xCuO_4$ (LSCO) [3] and OP YBCO [3] also shown by dotted lines in Figure 3. The

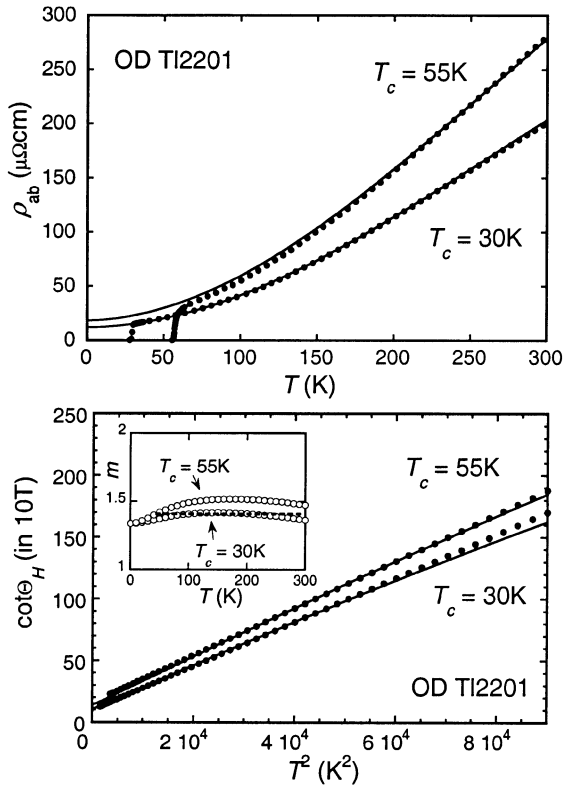


**Fig. 4.** Top: $\rho_{ab}(T)$ [22] (closed circles) and $\rho_{ab}^{fit}(T)$ (solid lines) for OD Tl2201 ($T_c$ = 55 K and $T_c$ = 30 K). Bottom: $\cot\Theta_H(T)$ [22] (closed circles) and $\cot\Theta_H^{fit}(T)$ (solid lines) for the same samples with the same fitting parameters (given in the text). Inset: $m^{fit}(T)$ (open circles) for the two sets of parameters. The dashed line represents the experimental data for the 30 K crystal [22].

open circles in the figure are $m^{fit}(T)$ for OP Tl2201 calculated using exactly the same model parameters that were used in Figure 2. As can be seen, $m(T)$ has the correct magnitude and $T$-dependence, decreasing by only 5% between 100 K and 300 K. Note that the present model does not include vertex corrections or paraconductivity contributions which might influence the form of $\Delta\rho_{ab}/\rho_{ab}(T)$, particularly at low $T$.

The behaviour of $m(T)$ is determined almost exclusively by the anisotropy parameters $c$ and $e$. (If $c = 0$, for example, $\Delta\rho_{ab}^{fit}/\rho_{ab}^{fit}$ would fall steeply as $T \rightarrow 0$). The large value of $e$ is striking, but is necessary, not only to give the correct magnitude for $m$ at finite temperatures, but also to maintain a robust $T^2$ dependence of $\cot\Theta_H(T)$. Hence, within this model, the observation of a quadratic Hall angle and the magnitude and $T$-dependence of the in-plane orbital MR are all signatures of a dominant and extremely anisotropic basal plane scattering rate varying as $T^2$. The $T$-linear resistivity is, on the other hand, simply a product of the broad crossover between the $T^2$ resistivity at low $T$ and the saturation of $\Gamma_{\rm eff}$ at higher temperatures.

The evolution with doping of the normal state transport properties in Tl2201 are summarized in Figure 4. The top panel in Figure 4 shows $\rho_{ab}(T)$ (closed circles) and $\rho_{ab}^{fit}(T)$ (solid lines) for two OD Tl2201 single crystals with $T_c$ values of 55 K and 30 K [22]. The fitting parameters used in these fits are $\alpha = 9$ THz, $\beta = 0.0016$ THz/K$^2$, $c = 2$ and $e = 11.5$ for the 55 K crystal, and $\alpha = 7$ THz, $\beta = 0.0015$ THz/K$^2$, $c = 2$ and $e = 8$ for the 30 K crystal. Note that all the anisotropy factors are markedly reduced here compared to OP Tl2201, effecting the increased curvature in $\rho_{ab}(T)$. The bottom panel in Figure 4 shows $\cot\Theta_H(T)$ and $\cot\Theta_H^{fit}(T)$ for the two samples. In contrast to OP Tl2201, $\cot\Theta_H^{fit}(T)$ deviates slightly from a simple $T^2$ dependence, being closer to $T^{1.95}$ and $T^{1.9}$ for the 55 K and 30 K crystals respectively. This deviation from $T^2$ dependence reflects the fact that in less anisotropic cuprates, extended regions of the Fermi surface begin to contribute to the Hall angle. The inset in the bottom panel of Figure 4 gives the modified Kohler's plot derived for the crystals. As we expect, $m^{fit}$ is smaller at these doping levels compared with OP Tl2201, with values approaching 1.55 and 1.4 for the 55 K and 30 K crystal respectively. Experimentally, $m = 1.4$ for 30 K Tl2201 (indicated by a dashed line) [22].

To conclude this section, I consider here briefly the possible effect of impurities on the transport properties of OP Tl2201, though I stress that any rigorous treatment of the effects of impurities is beyond the scope of this present paper, for a number of reasons. Firstly, although there have been numerous impurity studies carried out on HTSC, none to date have been carried out on OP Tl2201. Secondly, whilst Matthiessen's rule appears to be a robust feature of the physics of HTSC, it has been notoriously difficult to isolate the effects of impurity substitution from changes to the carrier concentration and, in the case of YBCO – the most heavily studied in this regard – the additional role of the chains. (Impurity substitution invariably leads to a small but significant increase in slope in $\rho_{ab}(T)$ presumably due to a change in the carrier density). Thirdly, different impurities are known to have significantly differing effects on the electronic environment within the basal planes, depending on whether the impurities are magnetic, or non-magnetic, are located within or away from the $CuO_2$ planes or whether the defects are point-like or extended, *e.g.* due to twinning or electron irradiation. Finally, as shown in Section 3.2, higher levels of disorder will often act to smear out some of the anisotropy in the scattering rate, making it extremely difficult to model any particular impurity study unambiguously within a single parameterization. With all these reservations in mind, I consider here only a simple and transparent treatment of the effects of impurities on $\rho_{ab}(T)$ and $\cot\Theta_H(T)$ in which multiples of $\alpha$ (*i.e.* 27, 54 and 81 THz) are inserted into the expression for $\Gamma_{\rm eff}$, keeping all other parameters fixed. The resultant $\rho_{ab}(T)$ and $\cot\Theta_H(T)$ are displayed in Figure 5.

Let us consider first $\rho_{ab}(T)$, shown in the top panel of Figure 5. Whilst Matthiessen's rule is obeyed reasonably well at low $T$, the presence of the shunt $\Gamma_{\rm max}$ begins to manifest itself at intermediate temperatures, causing the slope of the $T$-linear resistivity to fall with increasing

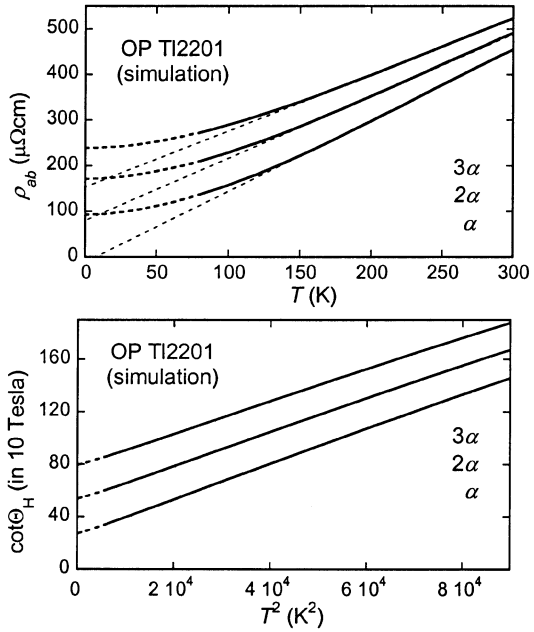


**Fig. 5.** Top: Simulated $\rho_{ab}(T)$ data for OP Tl2201 for different values of $\alpha$. The thin dashed lines are merely guides to the eye. Bottom: Corresponding plots of $\cot\Theta_H(T)$ for the same values of $\alpha$. All other parameters are the same as those used in Figures 2 and 3.

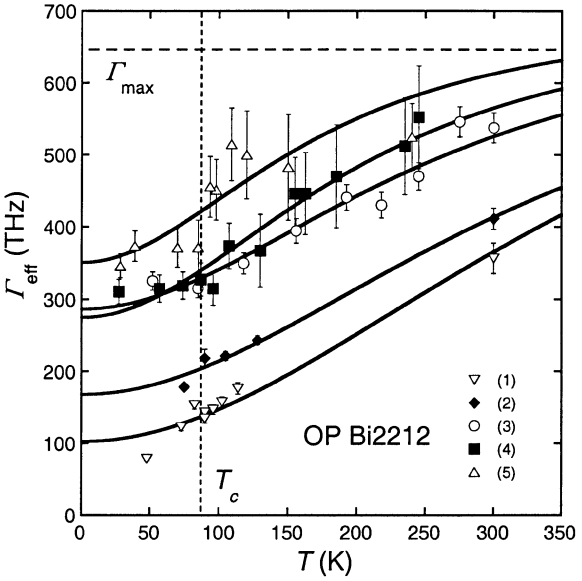


**Fig. 6.** Quasi-particle scattering rate for OP Bi2212 extracted from ARPES measurements [28]. The various numbers and symbols refer to different locations on the Fermi surface as identified in the text. The solid lines are our fits to the individual scattering rates using the expression for $\Gamma_{\rm eff}(\phi, T)$.

impurity concentration, in contrast to what is observed experimentally. (The thin dashed lines in Figure 5 show the extrapolations of these $T$-linear resistivities to 0 K.) For $\cot\Theta_H(T)$ on the other hand, Matthiessen's rule appears to be much more robust; increasing $\alpha$ simply produces a parallel shift in $\cot\Theta_H(T)$, the size of the shift being proportional to $\alpha$. This is to be expected since, as mentioned earlier, $\cot\Theta_H(T)$ is dominated by the behaviour of the nodal quasi-particles where $\Gamma_{\rm eff}$ is much smaller and thus much less influenced by the presence of $\Gamma_{\rm max}$. Of course, a full treatment of the effects of impurities on $\rho_{ab}(T)$ and $\cot\Theta_H(T)$ would have to consider any subsequent change in the anisotropy factors, which as discussed above in relation to OD Tl2201, will lead inevitably to a weakening of the $T$-dependence in $\cot\Theta_H(T)$. However, this example should serve as an illustration at least of both the capabilities and the limitations of this model in dealing with the full spectrum of normal state transport phenomena in HTSC.

### 3.2 Application to Bi2212

With its much improved energy and momentum resolution, ARPES has now become a powerful probe of the single-particle self-energy $\Sigma$ of HTSC. The vast majority of work to date has been carried out on the bilayer cuprate Bi2212, due to its ease of cleaving. One of the most striking features of the emerging spectral function in Bi2212 is the broad featureless normal state spectrum near ($\pi$, 0) that sharpens dramatically into the well-known peak-dip-hump structure upon cooling below $T_c$. Although interpretation of ARPES spectra remains controversial [26], it has been argued [7,27] that this broad normal state spectrum is a signature of ill-defined quasi-particle states rendered incoherent by some form of catastrophic low-energy scattering mechanism that is frozen out below $T_c$. The broadening of the quasi-particle self-energy is much less dramatic for quasi-particles at ($\pi$, $\pi$) while the basal plane anisotropy is far larger for OP cuprates than for OD cuprates [15]. All these features indicate a highly anisotropic normal state scattering rate which grows weaker with overdoping, consistent with the picture portrayed above for Tl2201.

Figure 6 shows the variation of the quasi-particle scattering rate with angle and temperature for OP Bi2212, extracted from the ARPES data of Valla *et al.* [28]. The various symbols used in Figure 6 are the same as those in the original plot of the momentum widths $\Delta k$, obtained by fitting Lorentzians to the different momentum distribution curves. The quasi-particle scattering rate $1/\tau$ is determined from the usual expression $1/\tau = |2{\rm Im}\Sigma| = \hbar\Delta k v_F$ where ${\rm Im}\Sigma$ is the imaginary part of the single-particle self energy and $v_F$ is the unrenormalized band velocity $\sim 4.0\times10^5$ ms$^{-1}$. The numbers refer to locations on the Fermi surface at angles $\phi$ of (1) 45°, (2) 37.5°, (3) 25.5°, (4) 17.5° and (5) 7° away from ($\pi$, 0).

The renormalised normal state Fermi velocities, obtained at each location from the slope of the dispersion relation near the Fermi level, can be approximated by the expression $v_F(\phi) = 2.5(1 + 0.2\sin^2 2\phi) \times 10^5$ ms$^{-1}$ [28]. Note that this is the same $v_F(\phi)$ used in the Tl2201 analysis. The solid lines in Figure 6 are the fits to the ARPES Bi2212 data using the model scattering

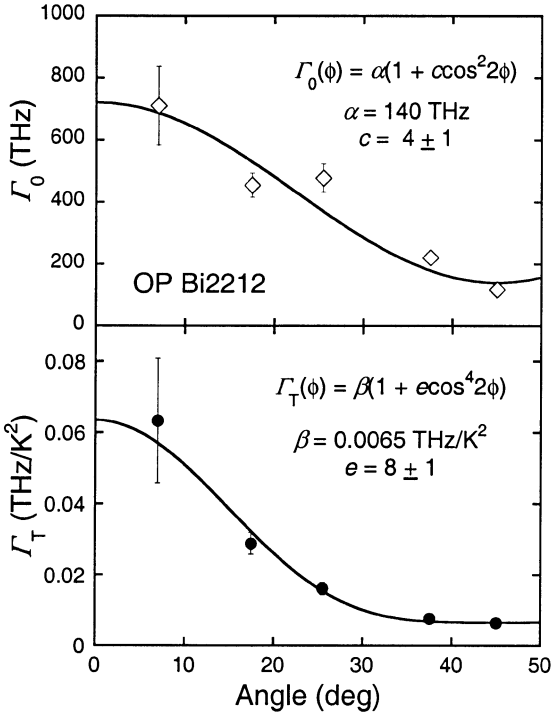


**Fig. 7.** Angular dependence of $\Gamma_0$ (top panel) and $\Gamma_T$ (bottom panel) for OP Bi2212 determined from the fits to the MDC curves given in Figure 5. The solid lines are best fits using the expressions shown in the appropriate figures.

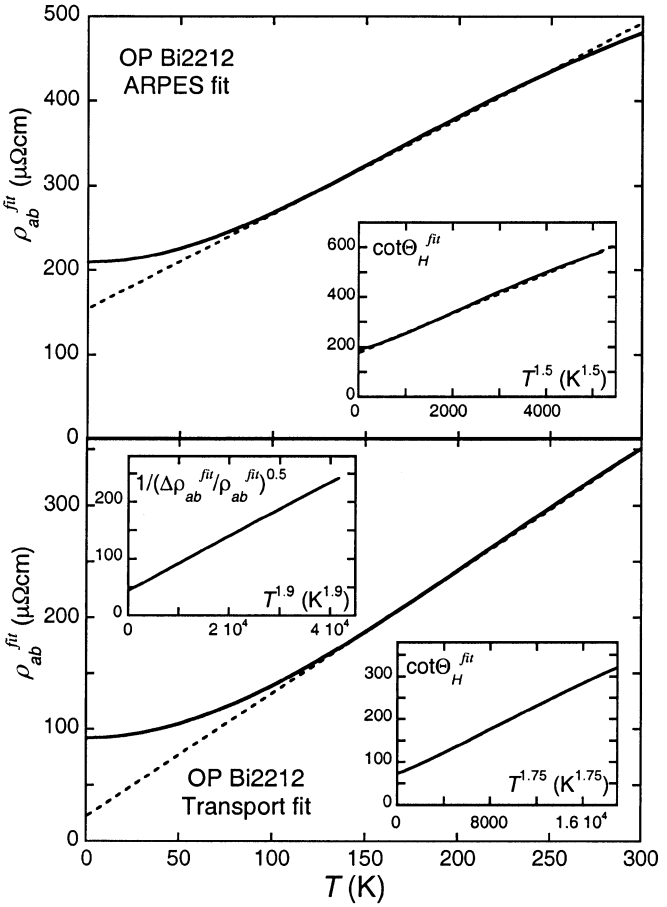


**Fig. 8.** Top panel: $\rho_{ab}^{fit}(T)$ and $\cot\Theta_H^{fit}(T)$ (inset) for OP Bi2212 using the fitting parameters derived from the ARPES data (see Fig. 6) . *Solid circles*: the results from the model, *dashed lines*: guides to the eye. Bottom panel: Comparable best fits to $\rho_{ab}(T)$ data [31] (main figure) and $\cot\Theta_H(T)$ data [31] (bottom inset) for OP Bi2212. The top inset shows the expected $T$-dependence of $1/(\Delta\rho_{ab}/\rho_{ab})^{0.5}(T)$ for the same parameters. Note the differing $T$-dependencies of the various plots.

rate $\Gamma_{\rm eff}(\phi, T)$ with $v_F(\phi) = 2.5(1{+}0.2\ \sin^2 2\phi){\times}10^5$ ms$^{-1}$ and $\Gamma_{\rm max}(\phi) = 650(1 + 0.2\ \sin^2 2\phi)$ THz or $0.45(1 + 0.2\ \sin^2 2\phi)$ eV. The fits are all reasonable and give angular dependencies for the resulting $\Gamma_0(\phi)$ and $\Gamma_T(\phi)$ as shown in Figure 7. The solid lines in Figure 7 are weighted fits to the expressions $\Gamma_0(\phi) = \alpha(1 + c\cos^2(2\phi))$ and $\Gamma_T(\phi) = \beta(1 + e\cos^4(2\phi))$ with $\alpha = 140$ THz, $\beta = 0.0065$ THz/K$^2$, $c = 4 \pm 1$ and $e = 8 \pm 1$. Note that $\Gamma_T(\phi)$ is somewhat more strongly peaked at $(\pi, 0)$ than is $\Gamma_0(\phi)$, making the functional forms of $\Gamma_T(\phi)$ and $\Gamma_0(\phi)$ slightly different. The reason these anisotropy factors seem large is the presence of $\Gamma_{\rm max}$. As $\Gamma_{\rm eff}(\phi, T)$ approaches $\Gamma_{\rm max}$, $\Gamma_{\rm ideal}(\phi, T)$ must change significantly in order to induce even a small change in $\Gamma_{\rm eff}(\phi, T)$. Hence within this model, the 'ideal' scattering rate is actually much more anisotropic than the raw data suggest.

The form of $\Gamma_{\rm eff}(\phi, T)$ obtained above, when inserted into the BTE, provides a crude estimate of $\rho_{ab}^{fit}(T)$ and $\cot\Theta_H^{fit}(T)$ as shown in the top panel of Figure 8. The resistivity displays a very large zero-temperature offset though it is approximately linear from $T_c$ up to $T = 250$ K at which point, $\rho_{ab}^{fit}(T)$ starts to saturate as the effect of $\Gamma_{\rm max}$ becomes prominent. $\cot\Theta_H^{fit}(T)$, on the other hand, is found to vary roughly as $A + BT^{1.5}$. Experimentally, $\rho_{ab}(T)$ in OP Bi2212 shows the ubiquitous $T$-linear behaviour, but in contrast to YBCO and Tl2201, has a large *positive* zero-temperature intercept, indicative of the increased structural inhomogeneity in this compound [29], whilst $\cot\Theta_H(T) = A + BT^n$ with $n = 1.75 \pm 0.05$ [14,30]. Similar behaviour has also been reported for Bi2201 [13,14].

Whilst the ARPES-derived fits are all reasonable, one does not expect the transport scattering rate to be equivalent to the single-particle scattering rate obtained by ARPES, because the former should be dominated by large-angle scattering events whilst the latter will not. The best actual fits to the experimentally determined transport data for OP Bi2212 [31] are given in the bottom panel of Figure 8 where the fitting parameters $\alpha = 50$ THz, $\beta = 0.00325$ THz/K$^2$, $c = 4$ and $e = 8$ were used. These values yield the expected linear resistivity between $T_c$ and 300 K with the correct slope and intercept, together with $\cot\Theta_H^{fit}(T) = A + BT^{1.75}$ *over the entire temperature range*, again with the correct slope and intercept. Taking the same parameters, $\Delta\rho_{ab}^{fit}/\rho_{ab}^{fit}(T)$ is found to vary as $(C + DT^{1.9})^{-2}$, as shown in the bottom panel of Figure 8. (This is only a prediction from the model at

the present time because $\Delta\rho_{ab}/\rho_{ab}(T)$ has yet to be established experimentally in OP Bi2212). The much larger residual scattering rate inferred from the ARPES spectra is a common feature of photoemission results [11]. Note though that $c$ and $e$ are unchanged, whilst $\beta$ in the transport fit is exactly half the ARPES value. The deviation of $\cot\Theta_H(T)$ from a simple $T^2$ dependence seems therefore to be a consequence of the increased structural disorder in Bi2212, reflected in $\rho_0$, that acts to smear out some of the anisotropy of the scattering rate around the Fermi surface.

The ARPES data of Valla *et al.* [28] are often cited as strong evidence for a *linear* quasi-particle scattering rate in HTSC that is itself responsible for the $T$-linear resistivity observed at optimal doping. However, as was noted by Valla and his co-workers, near the anti-nodal point (label number (5) in Fig. 6), the scattering rate becomes almost $T$-independent [28]. This tendency towards saturation near $(\pi, 0)$ is an essential feature of the present model, and combined with a single scattering rate that is *quadratic* in temperature *everywhere* on the Fermi surface, can account for the quasi-linear scattering rate at the nodes (Fig. 6), the $T$-linear resistivity, the tendency towards saturation at $(\pi, 0)$ and $\cot\Theta_H(T) \sim A + BT^{1.75}$, without requiring any additional assumptions. Clearly, in this regard, ARPES measurements on OP Tl2201 would provide a 'smoking gun', not only for the appropriateness of this model, but for other phenomenologies too. For the present analysis to be universally valid, for example, one should expect (i) a marked increase in the effective anisotropy $e^*$ between $(\pi, 0)$ and $(\pi, \pi)$ and (ii) a significant departure from linearity in the energy dependence of $\mathrm{Im}\Sigma$ for the nodal quasi-particles. By comparison, the scattering rate at the nodes in the 'Cold-Spots' model is uniquely quadratic [7], whilst in the MFL [9], there is no saturation at $(\pi, 0)$.

## 4 Discussion

Whilst many of the anomalous features seen in the normal state transport properties of HTSC can be reproduced by the simple phenomenology outlined above, the current proposal appears, at first sight at least, to be incompatible with two well-established aspects of the experimental situation in HTSC; namely the extension of the linear resistivity down to low $T$ and an absence of overt resistivity saturation at high $T$. Therefore, before going on to discuss the physical implications of the model, it is worth examining how these two major discrepancies might possibly be reconciled.

It often has been argued that $\rho_{ab}(T)$ in OP cuprates is linear at all finite temperatures. This long-held view is based largely on the remarkable observation back in 1990 of a linear $\rho_{ab}(T)$ in single crystal Bi2201 extending from 700 K right down to $T_c \sim 10$ K [32]. If this were indeed the intrinsic behaviour of all HTSC, it would certainly require an explanation beyond the realms of conventional FL physics. However, important new data on the latest generation of Bi2201 crystals (with significantly improved $T_c$ values) tell a rather different story. Upon suppressing superconductivity in OP Bi2201 ($T_c = 32$ K) in a 60 tesla pulsed magnetic field, Ono *et al.* [25] have found that the linear $\rho_{ab}(T)$ seen at high $T$ (and giving an apparent zero intercept at $T = 0$ K) in fact crosses over to a higher power $T$-dependence below around 60 K, before settling to some finite *positive* $\rho_0$. Similar behaviour has also been reported for OP LSCO [24]. Moreover, the (extrapolated) negative intercept in $\rho_{ab}(T)$ found in the best quality Tl2201 and YBCO crystals [21,33] is clearly unphysical and requires that $\rho_{ab}(T)$ *must* cross over to a higher power of $T$ at lower temperatures. Collectively, these findings suggest that fluctuation effects, evident in the $\rho_{ab}(T)$ data of Tl2201 and Bi2212, may be obscuring the intrinsic zero-field physics of OP LSCO and Bi2201 and lead to an apparent extension of the $T$-linear $\rho_{ab}(T)$ to unphysical limits. In this regard, it would be illuminating to follow $\rho_{ab}(T)$ in OP cuprates with higher $T_c$ down to lower temperatures, as and when larger magnetic fields become available.

I now turn to address the second point, namely the avoidance of resistivity saturation in HTSC at higher temperatures. The MIR limit and the parallel-resistor model have been applied successfully to a wide variety of materials. However, their relevance to strongly correlated electron systems such as HTSC has been challenged in recent times [34]. In these so-called 'bad metals', $\rho(T)$ does not saturate. Instead $\rho(T)$ continues to grow approximately linearly with $T$ at high temperatures (typically $T > 300$ K) attaining values of the order 1–10 m$\Omega$cm that correspond to $\ell \ll a$. Whilst the origin of non-saturating resistivity in these systems is still poorly understood, it has been claimed that the absence of resistivity saturation signals a non-FL ground state at zero temperature [34]. At first sight, this point of view appears rather compelling. Significantly however, a similar $\rho(T)$ behaviour has also been reported in $Sr_2RuO_4$ [35], a close structural analogue of the cuprates which forms a well-defined FL ground state at low $T$. Clearly, the quasi-particle description in $Sr_2RuO_4$, while valid at low $T$, must break down once the MIR limit is violated. Thus, the automatic association of non-saturating $\rho(T)$ with a non-FL ground state is misleading and some other physical origin for the high-$T$ behaviour should be sought.

Possible alternative sources for the 'excess resistivity' include thermal expansion effects (known to play a significant role in the organic conductors, for example), a thermally-induced reduction in the density of states or carrier concentration, and the onset of a 'thermal' diffusive (non-Boltzmann) transport regime at high $T$ setting in once the concept of a metallic scattering rate is no longer applicable and temperature becomes the only relevant energy scale in the problem. How quasi-particle transport crosses over from Boltzmann band-like transport to diffusive transport beyond the MIR limit is not well understood at the present time, though there is still much discussion of this important issue within the literature [36]. At high temperatures, one can employ the Kubo formalism to derive an exact expression for the

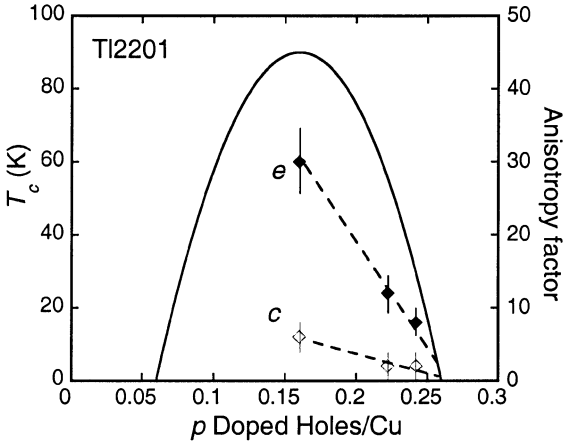


**Fig. 9.** Variation with doping concentration $p$ of the anisotropy factors $c$ (open diamonds) and $e$ (closed diamonds) for Tl2201. The dashed lines are guides to the eye. The solid line represents the $T_c(p)$ parabola for HTSC [40]. The error bars reflect the range of fitting parameters that provide a reasonable fit to all three transport coefficients.

resistivity, and some important results relating to the absence of resistivity saturation in the cuprates are emerging [37]. This formulism however has limited applicability in the low-temperature Boltzmann regime. In reality, as one crosses between the two extremes, it seems reasonable to expect a rather broad regime in temperature and/or frequency in which the Boltzmann equation is approximately correct and that the breakdown of applicability of the Boltzmann analysis will occur only very gradually, more so when one introduces anisotropy into the scattering rate. Determining the origin of this non-saturating resistivity, though clearly desirable, is not essential for verifying the model proposed here however, since currently, it is only strictly applicable in the low-$T$ ($T < 300$ K) regime, where the majority of the carriers are still well-defined quasi-particles and Boltzmann transport analysis remains (approximately) valid. However, the fact that a Boltzmann-type of analysis does seem to work so well in this regime suggests, to the author at least, that a coherent understanding of how Boltzmann analysis breaks down beyond the MIR limit is perhaps a more pressing issue than the deeper question of how a breakdown of FL theory in HTSC might be achieved.

Direct observation of a threshold in the scattering rate itself would obviously lend significant weight to the above arguments. Besides the work of Valla *et al.* [28], Norman *et al.* have also extracted Im$\Sigma$ along ($\pi$, 0) for slightly OD Bi2212 [27] and found that it too saturates above $T_c$. Optical measurements may also be used in principle to extract $\Gamma$ from the optical conductivity, though here the situation is not as clear. In particular, $\Gamma$ is observed to saturate with increasing temperature, but NOT with increasing frequency [38]. Finally, recent analysis of the plasmon spectra in $K_3C_{60}$ [39], another system with non-saturating resistivity, has revealed that the quasi-particle scattering rate saturates around $T = 500$ K at a value $\Gamma_{\rm max} \sim 0.5$ eV. Whilst more experimental work is clearly required to confirm this effect, the above observations do not rule out the possibility that the MIR limit is a preserve of *all* metallic systems, in the strict sense that $\Gamma$ never exceeds the maximum value $\Gamma_{\rm max}$ corresponding to $\ell = a$; the excess resistivity seen in strongly correlated systems ought not to be regarded therefore simply as a product of an ever-increasing scattering rate and further efforts to delineate $\Gamma(T)$ from $\rho(T)$ are strongly recommended.

Turning now to the physical implications of the model, the most striking features of the analysis for Tl2201 are clearly the large values for $c$ and $e$ and their strong variation with doping, as summarized in Figure 9. (For each crystal, the doping level $p$ is obtained from the well-known HTSC parabola law $T_c(p)/T_c^{\rm max} = 1 - 82(p - 0.16)^2$ [40], the solid line in Fig. 9.)

The large value of $c$, particularly at optimum doping, is somewhat surprising, though is not inconsistent with the picture emerging from ARPES measurements on Bi2212 [28]. Recently it has been argued [10] that scattering by impurities located *off* the $CuO_2$ planes may be the source of this four-fold anisotropy in $\Gamma_0(\phi)$. In the case of tetragonal Tl2201, such interplane randomness may derive from Tl/Cu site substitutions as well as the interstitial excess oxygen. However it is not clear at this stage why then such large anisotropy appears in the transport scattering rate, which typically depends only on large-momentum transfers. However, as noted by Varma and Abrahams [10], this peculiar elastic scattering contribution may well play a key role in the *magneto*-transport behaviour. Indeed, a large value of $c$ is required here solely to maintain the constancy of $m^{fit}(T)$ down to low temperatures.

The $T$-dependent anisotropy factor $e$ is found to drop steeply from optimal doping, scaling approximately with $T_c$ and approaching zero close to the doping level for which superconductivity vanishes. This is to be expected perhaps, because the separation of transport and Hall lifetimes is observed to vanish in the most highly OD samples [41]. The correlation between $e(p)$ and $T_c(p)$ on the OD side is significant and suggests that the mechanism giving rise to this large and strongly anisotropic scattering term might also be associated with the strength of the pairing interaction and the anisotropy ($d$-wave pairing symmetry) of the superconducting order parameter.

Comparison of the fitting parameters for OP Bi2212 and OP Tl2201 reveals another important aspect of the modelling. As was illustrated in Figure 1, ${\Gamma_{\rm ideal}}^{(\pi,0)}(T)$ for OP Tl2201 is found to cross the MIR limit close to $T = T_c$. The same is also true for OP Bi2212. (Whilst the degree of anisotropy in OP Bi2212 is markedly reduced compared with OP Tl2201, the coefficients $\alpha$ and $\beta$ are increased, making ${\Gamma_{\rm ideal}}^{(\pi,0)}(T)$ at $T = T_c$ very similar in the two cases.) The picture which emerges then from the transport analysis is one in which the quasi-particles at ($\pi$, 0) are fast approaching an incoherent state at $T = T_c$, consistent with the ARPES results. This breakdown of coherence at $T \sim T_c$ may well have implications for the onset temperature of superconductivity on the underdoped (UD) side of the phase diagram. Explicitly, if $e$ continues to grow with decreasing $p$, the temperature at which

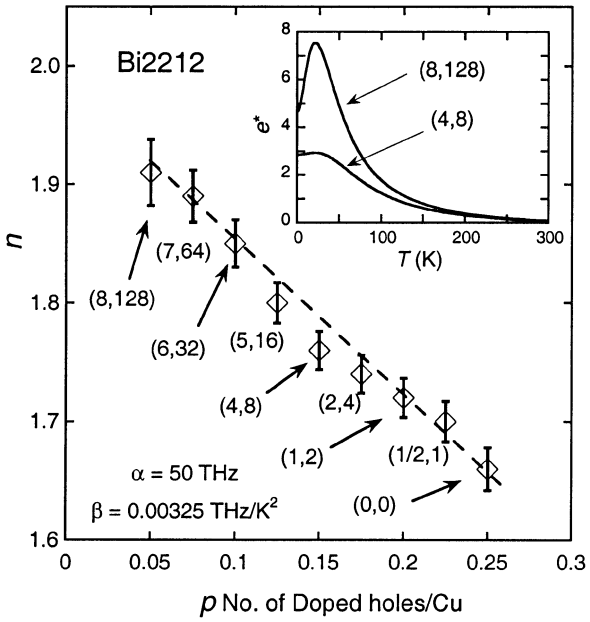


**Fig. 10.** Evaluation of the variation of $n(p)$ for Bi2212 where $n$ is the temperature exponent of inverse Hall angle $\cot\Theta_H(T) = A + BT^n$. The anisotropy factors ($c$, $e$) used in the fitting routines are indicated in parentheses. The dashed line is a guide to the eye [14]. Inset: Effective anisotropy $e^*(T)$ for two selected cases.

the anti-nodal quasi-particles become incoherent must decrease accordingly. What ultimately causes the suppression of $T_c$ on the UD side of the phase diagram is still an open issue, and we cannot resolve that important question here, since clearly, the physics of the UD cuprates is heavily influenced by the opening of the spin and charge pseudogap(s) which cannot yet be embraced within our simple phenomenological model. Nevertheless, the appearance of incoherent quasi-particles at $T = T_c^{\max}$ is a key result from the above analysis and hints at an alternative interpretation of the famous $T_c(p)$ parabola.

Further analysis of the Hall angle in Bi2212 does provide some possible insight, however, into the evolution of the scattering intensity on the UD side of the phase diagram. Detailed transport studies of the Bi-based cuprates Bi2212 and Bi2201 have shown that $\cot\Theta_H(T) \sim A + BT^n$ with $n$ decreasing from $n \sim 2$ to $n \sim 1.6$–$1.7$ as one moves from the UD to the OD regime [13,14,30]. This non-universal power law behaviour in $\cot\Theta_H(T)$ details the high level of complexity in the phenomenology of normal state transport in HTSC that has yet to be properly addressed. Given that at optimal doping, $n \sim 1.8$ lies roughly in the middle of the variable range for Bi2212, it is tempting to attribute this variation in $n(p)$ purely to changes in $c$ and $e$ across the phase diagram. A simple example of how this can be achieved is illustrated in Figure 10 where $c$ and $e$ have been varied systematically to simulate the experimentally observed variation of $n$ with doping [14], here keeping $\alpha$ and $\beta$ fixed at the values extracted from the transport fits for OP Bi2212 in Figure 8 (*i.e.* $\alpha = 50$ THz, $\beta = 0.00325$ THz/K$^2$). Intriguingly, for the fully isotropic case $c = e = 0$, $n \sim 1.65$. As $c$ and $e$ are increased, $n$ rises as expected, but approaches $n = 2$ only for extremely large values of $e$. Although this treatment is far from rigorous, it does suggest that with more detailed analysis, the systematic variation of $n$ with doping in Bi2212 and Bi2201, and its range of values, might be reproduced within the same picture. It implies also that the anisotropy of the $T^2$ scattering rate is going to increase (almost exponentially) with decreasing doping on the UD side, attaining values greater than 100 for $p \sim 0.05$! Within the present model, it is indeed the *only* way to account for the observation of $\cot\Theta_H(T) = A + BT^2$ in UD Bi2212. Nevertheless, as illustrated in the inset to Figure 10, the *effective* anisotropy $e^*(T)$ is almost indistinguishable for the OP and the most UD cases above 100 K. Hence, whilst $e$ may increase dramatically, the more experimentally accessible quantity $e^*$ will not.

Whilst I personally do not wish to speculate at this stage on the origin of $\Gamma_{\rm eff}(\phi, T)$, there are still some important remarks that can be made from the above analysis. Firstly, the strong anisotropy and $T^2$ dependence of $\Gamma_{\rm eff}(\phi, T)$ strongly implies that the dominant scattering rate in HTSC is electronic in origin and that electron-phonon scattering plays only a subsidiary role in the normal state transport properties of HTSC. The large increase in the quasi-particle lifetime below $T_c$ observed in thermal and electrical conductivity measurements [42,43] is consistent with the termination of such a catastrophic electronic scattering below $T_c$. Whether the disappearance of this catastrophic scattering could alone provide the energy imbalance necessary to account for high temperature superconductivity is an interesting open question [44], but it is intriguing to note that the energy scales required to account for the optical sum rule in OP HTSC are of the order of $\Gamma_{\max}$ ($\sim 0.16$–$0.5$ eV) [45]. Secondly, the large value for $e$ in OP Tl2201 (Fig. 9) implies the existence of a singular scattering mechanism, peaked at $(\pi, 0)$, the intensity of which grows rapidly with decreasing carrier concentration. Moreover, the hypothesized growth of the intensity of the scattering at $(\pi, 0)$ as we move towards localisation and the antiferromagnetic (AFM) state (Fig. 10) points to a scattering mechanism that is magnetic in origin, possibly due to some form of AFM spin fluctuations. Given the form of the anisotropy and its singular nature, the collective resonance mode evident in neutron scattering measurements on several cuprates, including Tl2201, is an attractive possibility. Intriguingly, whilst the resonance mode is resolution limited, *i.e.* strongly peaked at $(\pi, 0)$ in Tl2201 [46], it is significantly broadened in $Q$-space in Bi2212 [47], consistent with the conclusions derived above. It is noted however, that this mode has so far been unambiguously resolved only below $T_c$, so its relevance to scattering in the normal state has yet to be established.

## 5 Conclusions

In summary, I have demonstrated how the seemingly anomalous dc transport properties of HTSC may be accounted for consistently within a Boltzmann transport analysis with a unified $T^2$ scattering rate that varies

markedly around the basal plane. In particular, the separation of transport and Hall lifetimes, the modified Kohler's rule and the evolution of the transport properties across the OD region of the phase diagram can all be reproduced employing a single set of parameters. In addition, the different $T$-dependence of the Hall angle observed in the Bi-based cuprates is indicated to be an artefact of the increased structural inhomogeneity in these materials; the $T^2$ scattering rate continues to be the dominant source of scattering in Bi2212 but its singular form is smeared out by the disorder. The form of $\Gamma_{\rm eff}(\phi, T)$ is also consistent with several aspects of the single-particle spectral function revealed by ARPES, including the strong basal plane anisotropy (both in the zero-temperature and the $T$-dependent scattering terms) and the tendency towards saturation along $(\pi, 0)$. Such a wide-ranging consistency with experiment is encouraging and strongly endorses the notion that a conventional Boltzmann transport approach might be more applicable to the normal state transport properties of HTSC (at least in OP and OD cuprates) than was previously imagined.

The fact that the parent HTSC compound at half-filling is an AFM Mott insulator rather than a metal clearly sets the role of strong electron correlations in the square planar $CuO_2$ lattice as a key element in the cuprate problem. The introduction of holes into a highly correlated 2D magnetic background creates a non-FL ground state at low doping, characterized by the highly anomalous physics of the UD cuprates. Ultimately, this gives way to unconventional high temperature superconductivity. With continued doping, these systems eventually evolve into a conventional FL as the electron correlations become weaker and the material becomes more three-dimensional [48]. In this paper, a form for the normal state scattering rate has been identified that although unconventional (in respect of its absolute magnitude), is still rooted in a FL framework, yet can explain the evolution of the normal state transport properties of OD HTSC right back to optimum doping. Of course, one should not expect this simple model to remain valid on the UD side of the phase diagram, but if it truly applicable to the OD and OP cuprates, then the way in which this relatively simple picture breaks down, as the pseudogap opens and electron correlations become even stronger, might yet reveal the crucial missing link between the FL fixed point at large doping [48] and the curious physics of HTSC on the underdoped side.

The author would like to acknowledge enlightening discussions with J.F. Annett, K. Behnia, A. Carrington, J.R. Cooper, I.R. Fisher, B.L. Gyorffy, J.W. Loram, A.P. Mackenzie, N. Nagaosa, R. Ramazashvili, K.G. Sandemann, A.J. Schofield, H. Takagi, J.L. Tallon and J.A. Wilson, whose critical reading of the manuscript was gratefully received. The author also would like to acknowledge the hospitality of the University of Tokyo where many of these ideas were first formulated.

## Appendix: Transport coefficients for a quasi-2D Fermi surface

The current response $\boldsymbol{J}_i$ to an applied electric $\boldsymbol{E}$ is given by

$$\boldsymbol{J}_i = \frac{1}{4\pi^3}\int e\boldsymbol{v}_i g_k \mathrm{d}^3k = \sigma_{ij}\boldsymbol{E}_j$$

where $g_k$ is the displacement from the equilibrium distribution($g_k$ = $f$ - $f_0$) due to the applied fields, $\sigma_{ij}$ is the conductivity tensor and $v_i$ is the Fermi velocity in the $i$ direction. The total displacement can be summarized in the Bloch-Boltzmann transport equation, which under the relaxation time approximation, is given by

$$e\boldsymbol{E}\cdot\boldsymbol{v}_k\frac{\partial f_0}{\partial\varepsilon} + \frac{e}{\hbar}[\boldsymbol{v}_k\times\boldsymbol{B}]\frac{\partial g_k}{\partial k} = -g_k\Gamma.$$

The various components of $\sigma_{ij}^{(n)}$ can be obtained through the Jones-Zener expansion

$$g_k^{(n)} = \left(-\frac{e}{\hbar\Gamma}[\boldsymbol{v}_k\times\boldsymbol{B}]\frac{\partial}{\partial k}\right)^n\left(\frac{e\boldsymbol{E}\cdot\boldsymbol{v}_k}{\Gamma}\left(-\frac{\partial f_0}{\partial\varepsilon}\right)\right)$$

to arrive at:

$$\sigma_{ij}^{(n)} = \frac{1}{4\pi^3}\int ev_i\left(-\frac{e}{\hbar\Gamma}[\boldsymbol{v}_k\times\boldsymbol{B}]\frac{\partial}{\partial k}\right)^n\frac{ev_j}{\Gamma}\left(-\frac{\partial f_0}{\partial\varepsilon}\right)\mathrm{d}^3k.$$

To calculate, for instance, the in-plane Hall conductivity $\sigma_{xy}^{(1)}$, we simply apply $B_z$ and $E_y$ and calculate the response $J_x$ using the Jones-Zener term $g_k^{(1)}$.

For a quasi-2D Fermi surface, there are various techniques one can adopt to simplify the calculation. Firstly, the element $\mathrm{d}^3k$ is the product of an area parallel to the Fermi surface $\mathrm{d}S$ and a radial (in-plane) component $\mathrm{d}k_r$ which is related to an incremental energy $\mathrm{d}\varepsilon$ by

$$\mathrm{d}\varepsilon = \hbar v_F k_F = \hbar v_F\cos\gamma\mathrm{d}k_r.$$

Here $\gamma$ is the angle between $v_F$ and $\mathrm{d}k_r$ (within the plane). Since $v_F$ is always perpendicular to the Fermi surface, simple geometrical considerations give

$$\gamma(\phi) = \tan^{-1}\left[\frac{\partial}{\partial\phi}(\log k_F(\phi))\right]$$

which is zero for a circular Fermi surface.

The element $\mathrm{d}S$ can be expanded into the cylindrical elements $k_F\mathrm{d}\phi$ and $\mathrm{d}k_z$ to give

$$\int\left(-\frac{\partial f_0}{\partial\varepsilon}\right)\mathrm{d}^3k = \int_0^{2\pi}\int_{-\pi/d}^{\pi/d}\frac{k_F}{\hbar v_F\cos\gamma}$$

for a quasi-2D Fermi liquid since ($-\partial f_0/\partial\varepsilon$) is a delta function (provided all scattering is quasi-elastic). It is this integral $\int\mathrm{d}\phi$ that will contain all the in-plane anisotropy of the essential parameters in our calculation. With $B \parallel c$, the cross-product $[\boldsymbol{v}_k\times\boldsymbol{B}]\,\partial/\partial k$ becomes $Bv_F\partial/\partial k_\parallel$ where

$$\frac{\partial}{\partial k_\parallel} = \frac{\cos\gamma}{k_F}\frac{\partial}{\partial\phi}$$

whilst for $B \parallel ab$, making an angle $\varphi$ with the $a$-axis

$$[\boldsymbol{v}_k \times \boldsymbol{B}]\frac{\partial}{\partial k} = v_z[\hat{\boldsymbol{z}} \times \boldsymbol{B}]\frac{\partial}{\partial k_{xy}} + [\boldsymbol{v}_{xy} \times \boldsymbol{B}]\frac{\partial}{\partial k_z}$$

*i.e.*

$$[\boldsymbol{v}_k \times \boldsymbol{B}]\frac{\partial}{\partial k} \approx Bv_F \sin(\phi - \gamma - \varphi)\frac{\partial}{\partial k_z}.$$

Finally, it is noted that the tetragonal symmetry of Tl2201 allows the limits of integration to be reduced to 0 and $\pi/2$ by including an extra factor of 4.

Employing these simple techniques, one can now derive the individual terms of the in-plane and $c$-axis conductivity tensors. In this paper however, only the in-plane magneto-transport properties are considered and their formulae are listed below in the isotropic case. For the anisotropic case, simply replace $v_F$, $k_F$ and $\Gamma$ by $v_F(\phi)$, $k_F(\phi)$ and $\Gamma(\phi)$, or more appropriately for the present model, by $\Gamma_{\rm eff}(\phi, T)$.

$$\sigma_{xx}^{(0)} = \frac{e^2}{4\pi^3\hbar}\left(\frac{2\pi}{d}\right)4\int_0^{\pi/2}\frac{k_F v_F \cos^2(\phi-\gamma)}{\Gamma\cos\gamma}\mathrm{d}\phi$$

$$\sigma_{xy}^{(1)} = \frac{-e^3B}{4\pi^3\hbar^2}\left(\frac{2\pi}{d}\right)4\int_0^{\pi/2}\frac{v_F}{\Gamma}\cos(\phi-\gamma)\frac{\partial}{\partial\phi} \times \left(\frac{v_F}{\Gamma}\sin(\phi-\gamma)\right)\mathrm{d}\phi$$

$$\sigma_{xx}^{(2)} = \frac{e^4B^2}{4\pi^3\hbar^3}\left(\frac{2\pi}{d}\right)4\int_0^{\pi/2}\frac{v_F}{\Gamma}\cos(\phi-\gamma) \times \frac{\partial}{\partial\phi}\left\{\frac{v_F\cos\gamma}{\Gamma k_F}\frac{\partial}{\partial\phi}\left(\frac{v_F}{\Gamma}\cos(\phi-\gamma)\right)\right\}\mathrm{d}\phi.$$

The measurable quantities $\rho_{ab}$, $\tan\Theta_H$ and $\Delta\rho_{ab}/\rho_{ab}$ are obtained by inversion of the conductivity tensor:

$$\rho_{ab} = \frac{1}{\sigma_{xx}^{(0)}}$$

$$\tan\Theta_H = \frac{\rho_{xy}}{R_H B} \approx \frac{\sigma_{xy}^{(1)}}{\sigma_{xx}^{(0)}}$$

$$\frac{\Delta\rho_{ab}}{\rho_{ab}} = -\frac{\sigma_{xx}^{(2)}}{\sigma_{xx}^{(0)}} - \left(\frac{\sigma_{xy}^{(1)}}{\sigma_{xx}^{(0)}}\right)^2.$$

## References


1. M. Gurvitch, A.T. Fiory, Phys. Rev. Lett. **59**, 1337 (1987)
2. T.R. Chien, Z.Z. Wang, N.P. Ong, Phys. Rev. Lett. **67**, 2088 (1991)
3. J.M. Harris, Y.F. Yan, P. Matl, N.P. Ong, P.W. Anderson, T. Kimura, K. Kitazawa, Phys. Rev. Lett. **75**, 1391 (1995)
4. A. Carrington, A.P. Mackenzie, C.T. Lin, J.R. Cooper, Phys. Rev. Lett. **69**, 2855 (1992)
5. B.P. Stojkovic, D. Pines, Phys. Rev. Lett. **76**, 811 (1996)
6. C. Castellani, C. di Castro, M. Grilli, Phys. Rev. Lett. **75**, 4650 (1995)
7. L.B. Ioffe, A.J. Millis, Phys. Rev. B **58**, 11631 (1998)
8. P.W. Anderson, Phys. Rev. Lett. **67**, 2092 (1991)
9. C.M. Varma, P.B. Littlewood, S. Schmitt-Rink, E. Abrahams, A.E. Ruckenstein, Phys. Rev. Lett. **63**, 1996 (1989)
10. C.M. Varma, E. Abrahams, Phys. Rev. Lett. **86**, 4652 (2001)
11. T. Valla, A.V. Fedorov, P.D. Johnson, B.O. Wells, S.L. Hulbert, Q. Li, G.D. Gu, N. Koshizuka, Science **285**, 2110 (1999)
12. P.D. Johnson *et al.*, Phys. Rev. Lett. **87**, 177007 (2001)
13. Y. Ando, T. Murayama, Phys. Rev. B **60**, R6991 (1999)
14. Z. Konstantinovic, Z.Z. Li, H. Raffy, Phys. Rev. B **62**, R11989 (2000)
15. Z.M. Yusof, B.O. Wells, T. Valla, A.V. Fedorov, P.D. Johnson, Q. Li, C. Kendziora, Sha Jian, D.G. Hinks, Phys. Rev. Lett. **88**, 167006 (2002)
16. N.E. Hussey, J.R. Cooper, J.M. Wheatley, I.R. Fisher, A. Carrington, A.P. Mackenzie, C.T. Lin, O. Milat, Phys. Rev. Lett. **76**, 122 (1996)
17. N.P. Ong, Phys. Rev. B **43**, 193 (1991)
18. Z. Fisk, G.W. Webb, Phys. Rev. Lett. **36**, 1084 (1976)
19. H. Wiesmann, M. Gurvitch, H. Lutz, A. Ghosh, B. Schwarz, M. Strongin, P.B. Allen, J.W. Halley, Phys. Rev. Lett. **38**, 782 (1977)
20. M. Gurvitch, Phys. Rev. B **24**, 7404 (1981)
21. A.W. Tyler, A.P. Mackenzie, Physica C **282-287**, 1185 (1997)
22. A.W. Tyler, Ph.D. thesis (University of Cambridge, 1997)
23. D.J. Singh, W.E. Pickett, Physica C **203**, 193 (1992)
24. G.S. Boebinger, Y. Ando, A. Passner, T. Kimura, M. Okuya, J. Shimoyama, K. Kishio, K. Tamasaku, N. Ichikawa, S. Uchida, Phys. Rev. Lett. **77**, 5417 (1996)
25. S. Ono, Y. Ando, T. Murayama, F.F. Balakirev, J.B. Betts, G.S. Boebinger, Phys. Rev. Lett. **85**, 638 (2000)
26. See, *e.g.*, S.V. Borisenko, A.A. Kordyuk, S. Legner, C. Dürr, M. Knupfer, M.S. Golden, J. Fink, K. Nenkov, D. Eckert, G. Yang, S. Abell, H. Berger, L. Forr, B. Liang, A. Maljuk, C.T. Lin, B. Keimer, Phys. Rev. B **64**, 0904513 (2001)
27. M.R. Norman, M. Randeria, H. Ding, J.C. Campuzano, Phys. Rev. B **57**, 11093 (1998)
28. T. Valla, A.V. Fedorov, P.D. Johnson, Q. Li, G.D. Gu, N. Koshizuka, Phys. Rev. Lett. **85**, 828 (2000)
29. T. Watanabe, T. Fujii, A. Matsuda, Phys. Rev. Lett. **79**, 2113 (1997)
30. B. Beschoten, U. Rüdiger, J. Auge, C. Quitmann, H. Frank, H. Kurz, G. Güntherodt, Physica C **235-240**, 1373 (1994)
31. The $\rho_{ab}(T)$ data used to fit with the model were the $\delta = 0.255$ data in Figure 2 of reference [29]. The $\cot\Theta_H(T)$ data were the $p = 0.16$ sample shown in Figure 3 of reference [14]
32. S. Martin, A.T. Fiory, R.M. Fleming, L.F. Schneemeyer, J.V. Waszczak, Phys. Rev. B **41**, 846 (1990)
33. K. Yoshida, A.I. Rykov, S. Tajima, I. Terasaki, Phys. Rev. B **60**, R15035 (1999)

34. V.J. Emery, S.A. Kivelson, Phys. Rev. Lett. **74**, 3253 (1995)
35. A.W. Tyler, A.P. Mackenzie, S. NishiZaki, Y. Maeno, Phys. Rev. B **58**, R10107 (1998)
36. See, for example, B.K. Nikolic, P.B. Allen, Phys. Rev. B **63**, 020201(R) (2001)
37. M. Calandra, O. Gunnarsson, Phys. Rev. B **66** 205105 (2002)
38. A.V. Puchkov, D.N. Basov, T. Timusk, J. Phys. Cond. Matt. **8**, 10049 (1996)
39. A. Goldoni, L. Sangaletti, F. Parmigiani, G. Comelli, G. Paolucci, Phys. Rev. Lett. **87**, 076401 (2001)
40. J.L. Tallon, C. Bernhard, H. Shaked, R.L. Hitterman, J.D. Jorgensen, Phys. Rev. B **51**, 12911 (1995)
41. A.P. Mackenzie, S.R. Julian, D.C. Sinclair, C.T. Lin, Phys. Rev. B **53**, 5848 (1996)
42. R.C. Yu, M.B. Salamon, J.P. Lu, W.C. Lee, Phys. Rev. Lett. **69**, 1431 (1992)
43. D.A. Bonn, R. Liang, T.M. Riseman, D.J. Baar, D.C. Morgan, K. Zhang, P. Dosanjh, T.L. Duty, A. MacFarlane, G.D. Morris, J.H. Brewer, W.N. Hardy, C. Kallin, A.J. Berlinsky, Phys. Rev. B **47**, 11314 (1993)
44. J.E. Hirsch, Science **295**, 2226 (2002)
45. A.F. Santander-Syro, R.P.S.M. Lobo, N. Bontemps, Z. Konstantinovic, Z. Li, H. Raffy, Phys. Rev. Lett. **88**, 097005 (2002)
46. H.F. He, P. Bourges, Y. Sidis, C. Ulrich, L.P. Regnault, S. Pailhes, N.S. Berzigiarova, N.N. Kolesnikov, B. Keimer, Science **295**, 1045 (2002)
47. H.F. Fong, P. Bourges, Y. Sidis, L.P. Regnault, A. Ivanov, G.D. Guk, N. Koshizuka, B. Keimer, Nature **398**, 588 (1999)
48. S. Nakamae, K. Behnia, N. Mangkorntong, M. Nohara, H. Takagi, S.J.C. Yates, N.E. Hussey, `cond-mat/0212283` (2002)